

Explicit- and Implicit-Solvent Molecular Dynamics Simulations of Complex Formation between Polycations and Polyanions

Nazish Hoda* and Ronald G. Larson

Department of Chemical Engineering, University of Michigan, Ann Arbor, Michigan 48109

Received July 23, 2009; Revised Manuscript Received September 4, 2009

ABSTRACT: Explicit- and implicit-solvent molecular dynamics simulations are performed to study complexation in two polyelectrolyte systems: poly(styrene sulfonate)/poly(allylamine hydrochloride) (PSS/PAH) and poly(acrylic acid)/poly(allylamine hydrochloride) (PAA/PAH). Both these systems have been used in layer-by-layer assembly of polyelectrolyte films, with the first of these typically yielding linear growth in film thickness with increasing numbers of layers and the second yielding exponential growth. In both the systems, the polyelectrolytes have the same number of monomers and are present in stoichiometric proportion, and water is used as solvent. Simulations give important insights into the structure and composition of the complexes. We found that the PSS/PAH complex is more compact and has a smaller fraction of water than the PAA/PAH complex due to the presence of phenyl rings in the PSS chain and the hydrophilic nature of the charged group in the PAA chain. Either an increase in salt concentration or a decrease in partial charge fraction increases swelling and the water content in the complex. To overcome the computational limitations associated with the explicit-solvent simulation, a simple strategy to develop the force field for an implicit-solvent simulation is proposed. In the absence of salt and for fully charged polyelectrolytes, the radius-of-gyration and the various radial distribution functions predicted by the implicit-solvent simulation match well with those predicted by the explicit-solvent simulation, while reasonable agreement is obtained in the other cases. The implicit-solvent simulation was performed for bigger system sizes, and we observed trends similar to those observed for smaller system sizes, suggesting that the simulation results are independent of system size.

1. Introduction

The formation and properties of polyelectrolyte complexes are of great interest and importance in many fields, including paper-making, coatings, layer-by-layer (LbL) assembly,^{33,34} and gene therapy.³⁵ A number of researchers, including Kabanov and co-workers,^{36,37} as well as Dautzenberg and co-workers,^{38,39} have experimentally studied the kinetics and structure of complexes formed at different salt concentrations. Besides experiments, various coarse-grained models^{40,41} and simulations^{42–44} have been used to study polyelectrolyte complexation and have greatly enhanced our understanding about complexation. However, coarse-grained models cannot distinguish between polyelectrolytes with different structures, different types of salt ions, counterions and co-ions, and different solvents.

This limitation of typical coarse-grained models is especially constraining for the study of polyelectrolyte complexes that form during LbL assembly, which is the sequential adsorption of negatively and positively charged polyelectrolytes onto a charged substrate. In the last two decades, LbL has emerged as a versatile method for the assembly of a wide variety of films, including nanostructured materials that have shown promise for photovoltaic,^{1–12} fuel cell,^{13–16} and biomedical^{17–32} applications. Two types of LbL growth behavior have been reported in the literature, which are sensitive to molecular details not readily captured by coarse-grained models. Films deposited using poly(styrene sulfonate) and poly(allylamine hydrochloride) (PSS/PAH)^{45,46} and poly(styrene sulfonate) and poly(diallyldimethylammonium) (PSS/PDDA)⁴⁵ at room temperature and at low salt

concentrations are two examples of linearly growing films, where the film thickness, H , increases linearly with the number of deposited bilayers, N . Typical examples of films exhibiting exponential growth, where H increases exponentially with N , are hyaluronic acid/poly(L-lysine) (HA/PLL)^{47–50}, poly(L-glutamic acid)/poly(L-lysine) (PGA/PLL)^{46,51}, poly(L-glutamic acid)/poly(allylamine hydrochloride) (PGA/PAH),⁵² and hyaluronic acid/chitosan.⁵³ However, it has been reported that changes in salt concentration,⁵⁴ type of salt,^{55,56} solution pH,^{57–61} temperature,^{62,63} solvent quality,⁶⁴ and the properties of polyelectrolytes involved in assembly^{65–68} can change the growth behavior from linear to exponential or vice versa. In most cases, the exponential growth is attributed to the ability of at least one of the polyelectrolytes to diffuse in and out of the film.^{48,50} Recently, we proposed a one-dimensional model to describe the exponential growth and showed that films grow exponentially only when $Dt_d/H^2 \gg 1$, where D is the diffusivity of the polyelectrolytes in the film and t_d is the dipping time.⁶⁹ It is noteworthy that D is strongly dependent on film properties, which are influenced by the assembly conditions and the properties of polyelectrolytes involved in the deposition. Hence, it is of paramount importance to investigate how the factors mentioned above affect the structure and polyelectrolyte diffusivity in polyelectrolyte complexes, such as those that are formed during LbL deposition.

Coarse-grained, MD, and Monte Carlo simulations have been used in the past to study LbL assembly and to probe the role of electrostatic and nonelectrostatic interactions.^{70–73} A common finding of these studies is that there is a substantial intermixing between chains adsorbed during different deposition steps. The MD simulations of Sharkh also predict that layer thickness is independent of chain length,⁷¹ and simulations of Dobrynin and

*Corresponding author. E-mail: nazish.hoda@gmail.com.

co-workers predict that when the polyelectrolyte(s) involved in LbL assembly is(are) weakly charged the deposited layers are relatively thicker.⁷² Furthermore, Patel et al. proposed that the film growth is stable only when $\delta Q/Q = 0.5$, where Q is the total charge carried by the adsorbing chains and δQ is the net charge left on the film once adsorption is complete.⁷³ Film growth would eventually stop when $\delta Q/Q < 0.5$ and exponential increase in film thickness is expected when $\delta Q/Q > 0.5$. Although coarse-grained simulations have enhanced our understanding about LbL assembly, they cannot distinguish between polyelectrolytes with different structures, different types of salt ions, counterions and co-ions, and different solvents. One way to overcome these limitations is to perform atomistic MD simulations, where structural details and solvent are explicitly included.

With the present computational power, atomistic simulation of LbL assembly is infeasible. An analogous problem that can provide information directly or indirectly relevant to LbL assembly and also be studied using atomistic simulation is complex formation between polyelectrolytes. In recent years, attempts have been made to link LbL deposition to polyelectrolyte complexation, and many important connections between the two have been established.^{74–77} It was speculated by Kovacevic et al. that films deposited from polyelectrolytes forming weak complexes may exhibit exponential growth.⁷⁵ Later on, Laugel et al.⁷⁶ performed microcalorimetry experiments on several polyanion/polycation systems and found that a positive heat of complexation (endothermic) is characteristic of an exponential film growth and a negative heat of complexation (exothermic) is characteristic of a linear film growth. Furthermore, our model suggested that exponential growth results from higher diffusion rates.⁶⁹ An important goal of our simulation effort is to understand how the chemical structure of polyelectrolytes involved in complex formation affects the structure of resulting complex and as a consequence diffusion rates.

We report here explicit- and implicit-solvent simulations to study complexation in two different polyelectrolyte systems: PSS/PAH and PAA/PAH. Note, LbL films deposited using PSS/PAH typically grow linearly in aqueous conditions,^{46,78} while films deposited using PAA/PAH could grow exponentially.^{65,68} We expect that by studying complexation in these system the factors responsible for the difference in their growth behavior can be identified. The rest of the paper is organized in the following manner. In section 2, the molecular force fields employed for the three polyelectrolytes and explicit-solvent, atomistic simulation method are discussed. The results of explicit-solvent simulations, that is, the effects of number of monomers, salt concentration, and the degree of ionization on the properties of the two complexes, are presented and discussed in section 3. In section 4, the strategy adopted for developing the force field for the implicit-solvent simulation is explained, and the results of these simulations are presented. Finally, the key findings are summarized in section 5.

2. Models and Methods

2.1. Force Fields. Like previous atomistic MD simulation studies, the total potential energy of a system is represented as a sum of van der Waals, Coulombic, bond stretching, angle bending, and dihedral energy terms. The van der Waals interactions are described using Lennard-Jones (LJ) potential:

$$U_{LJ}(r) = 4\epsilon \left[\left(\frac{\sigma}{r} \right)^{12} - \left(\frac{\sigma}{r} \right)^6 \right] = \left[\frac{C_{12}}{r^{12}} - \frac{C_6}{r^6} \right] \quad (1)$$

where σ and ϵ are the length and energy parameters. In the above equation, C_6 and C_{12} are the parameters for the attractive and repulsive parts of LJ potential, respectively.

In this study, bonds are either kept rigid using LINCS algorithm⁷⁹ or a harmonic potential is used of the form:

$$U_{\text{bond}}(r) = \frac{1}{2} k_b (r - b)^2 \quad (2)$$

where k_b is the force constant, and r and b are the bond length and the equilibrium bond length, respectively. A harmonic potential is used to describe bond angle bending:

$$U_{\text{bending}} = \frac{1}{2} k_\theta (\theta - \theta_0)^2 \quad (3)$$

where k_θ is the bond bending force constant, and θ and θ_0 are the bond angle and the equilibrium bond angle, respectively. Depending upon dihedral angle, the dihedral energy term is described by either the Ryckaert-Bellmans (RB) potential⁸⁰, a proper dihedral potential, or an improper dihedral potential.

In this study, a united-atom force field is used. Below, we describe the force-field parameters used for the three polyelectrolytes.

2.1.1. PSS Force-Field Parameters. The PSS chain is modeled in a manner similar to that described in Vishnyakov and Neimark.⁸¹ There are nine distinct groups (include atoms and united atoms) in the PSS chain: CH, CH₂, CH₃, C1, C2, CH1, CH2, S, and O, and each PSS monomer contains a total of 12 of these groups. The LJ parameters for S and O are taken from ref 82, and for the rest of the groups the parameters are taken from ref 83. Table 1 lists the point charges on a PSS monomer; the assigned point charges are the same as those estimated by Vishnyakov and Neimark⁸¹ using an ab initio calculation.

All the covalent bonds in the PSS chain are assumed to be stiff and the potential given in eq 2 is used to maintain the bond lengths near their equilibrium values. Note, we also performed a simulation where all the bonds were made rigid and found that a very small time-step is required (≈ 0.2 fs) to achieve reasonable convergence. For C2—S and S=O bonds as well as (C2)SO and OSO angles, we use the potential parameters given in ref 81, while the parameters for the rest of the bonds and angles are taken from ref 83. We use the RB torsional potential to describe the rotation along the bonds in the aliphatic backbone, and (CH₂)(C2)SO torsion that determines the rotation of the sulfonate group around the (C2)—S bond. The RB torsional potential parameters for the two torsions are taken from refs 83 and 81, respectively. The phenyl ring is kept in a plane using an improper torsion potential:

$$U_{\text{impr}}(\phi) = \frac{1}{2} k_{\text{impr}} (\phi - \phi_0)^2 \quad (4)$$

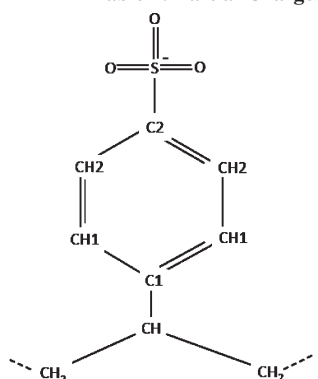
where ϕ is the torsion angle. Values for the constants k_{impr} and ϕ_0 are taken from ref 81.

To verify the accuracy of the above force field, we compared the radius-of-gyration, R_g , predicted by our simulation with a prior experiment. Wang and Hu found that the persistence length, l_p , of PSS in very dilute NaCl salt is 1.4 nm.⁸⁴ For this l_p , R_g was evaluated using the following expression:

$$R_g = l_p^2 \left[\frac{x}{3} - 1 + \frac{2}{x} - \left(\frac{2}{x^2} \right) (1 - \exp(-x)) \right] \quad (5)$$

where $x = L/l_p$ and L is the contour length. For 10- and 20-mer chains, $R_g = 0.66$ and 1.09 nm, respectively. For 10- and 20-mer chains, our simulation predicts R_g values of 0.74 ± 0.003 and 1.11 ± 0.003 nm, which match closely with the above predictions. (Note, in the simulations for 10- and 20-mer chains, we included 750 and 2000 water molecules, and the simulations were carried out for 10 ns.) We also found that the various radial distribution functions predicted by our simulation are in excellent agreement with those in ref 81 (not shown). The accord

Table 1. Partial Charges on a PSS Monomer in Units of Charge on an Electron

			
Group	Charge(e)	Group	Charge(e)
CH	0	CH ₂₍₃₎	0
C1	-0.03	C2	-0.23
CH1	-0.02	CH2	-0.1025
S	1.755	O	-0.75

between the predictions of our simulation and prior experimental and simulation studies gives confidence that the force field is reasonable. It is noteworthy that the true validity of any force field can only be established by performing simulations for large system sizes for hundreds of microseconds, which is presently infeasible because of computational limitations.

2.1.2. PAA and PAH Force-Field Parameters. Tables 2 and 3 list the force-field parameters for the PAA and PAH chains. The PAA chain has five different groups: CH, CH₂, CH₃, C, and O, and each PAA monomer contains five of these groups as shown in Table 2. In the case of PAH, there are six different groups: CH, CH₂, CH_{2N}, CH₃, N, and H, and each monomer contains seven of these groups. For both the chains, the aliphatic backbone is modeled using the GROMACS united-atom model.^{85,86} The point charges as well as the LJ parameters for the groups C and O in PAA (carboxyl group) are taken from the ENCAD force field,⁸⁷ and the CHARMM force field⁸⁸ is used for the groups N and H in PAH (amine group). All the covalent bonds in the PAA and PAH chains are kept rigid using the LINCS method; the equilibrium bond lengths for all the covalent bonds in the chains are listed in the above tables. We also performed simulations by replacing all the rigid bonds with stiff bonds. But this switch over does not lead to much improvement in the computational performance because of the relatively simple linear structure of the two chains. The bending potential parameters for the aliphatic backbone are taken from the GROMACS force field, for the CH–C–O and O–C–O angles (PAA) are taken from the ENCAD force field, and for the CH_{2N}–N–H and H–N–H angles (PAH) are taken from the CHARMM force field. As in the case of PSS, we use the RB torsional potential to describe the rotation along the bonds in the aliphatic backbone. The coefficients of the RB potential⁸⁹ are listed in the tables. For the other torsions, we use the following proper torsion potential:

$$U_{\text{proper}}(\phi) = k_{\text{proper}}(1 + \cos[n\phi + \phi_0]) \quad (6)$$

where k_{proper} is the torsion force constant. The parameters, n and ϕ_0 , for the CH₂–CH–C–O and CH–CH₂–CH–C torsions (PAA) are taken from ref 87, and for the CH₂–CH–CH_{2N}–N and CH–CH_{2N}–N–H torsions (PAH) are taken from ref 88.

We performed two different checks to ensure that the predictions of the above force fields are reasonable. First, we switched the force field for the carboxyl group in PAA from ENCAD to OPLS⁹⁰ and for the amine group in PAH from CHARMM to OPLS. The radius-of-gyration predicted by the new force field was very similar to that predicted by the old force field. For example, the ENCAD force field predicts that R_g for a 30-mer PAA chain is 1.18 ± 0.03 nm, and the OPLS force field predicts R_g value of 1.15 ± 0.01 nm. For a 30-mer PAH chain, both the force fields predict R_g value of 1.48 ± 0.04 nm. These simulations were carried out for 10 ns, and we included 1000, 2000, and 4000 water molecules for 10-, 20-, and 30-mer chains. Second,

we compare the R_g values predicted by our simulation with those reported in previous experimental and simulation studies. The radii-of-gyration of 8-, 12-, and 23-mer PAA chains were computed by Reith et al.⁹¹ using atomistic simulations. For 10- and 20-mer PAA chains, the interpolation of the data of Reith et al. yields R_g values of 0.66 and 1.06 nm, and these values match with the predictions of our simulation ($R_g = 0.66 \pm 0.02$ and 0.98 ± 0.01 nm for 10- and 20-mer chains). For PAH, to the best of our knowledge, the smallest molecular weight for which R_g was experimentally determined was 75 kDa.⁹² Extrapolation of this result to 10- and 20-mer chains gives R_g values of 0.6 and 1 nm. These estimates are in close proximity to the R_g values of 0.62 ± 0.01 and 0.94 ± 0.04 nm, predicted by our simulation.

In the present study, SPC water is used as solvent⁹³ and the water geometry is constrained using the SETTLE algorithm.⁹⁴ All the counterions and salt ions are modeled as charged Lennard-Jones centers, and the LJ parameters for all the ions are taken from the GROMACS force field.

2.2. Simulation Details. All the simulations were performed using the GROMACS simulation engine (version 3.3.1).⁹⁵ The initial configuration is generated by placing fully stretched polyelectrolytes in a cubic box along with randomly distributed counterions, salt ions (if required), and SPC water molecules. In all the simulations, the oppositely charged polyelectrolytes were kept 2 nm apart and were positioned such that they lie 1 nm away from the middle of the box. We also performed simulations where the oppositely charged polyelectrolytes were kept further apart. Although increasing the separation distance increases the complex formation time, the structural properties of the resulting complex remain almost the same. (In the absence of salt, when the oppositely charged polyelectrolytes are kept 2 nm apart, the complexes are formed during the first 2–3 ns.) The initial configuration is energy minimized to keep the maximum force on any group in the system below 100 kJ/nm mol. We used the steepest gradient method for the energy minimization, and a maximum displacement of 0.005 nm is used. MD simulation is performed on the energy minimized system under isothermal–isobaric (NPT) conditions, and a pressure of 1 bar and a temperature of 300 K are maintained during the simulation using the Berendsen coupling scheme.⁹⁶ Isotropic coupling is applied and temperature and pressure coupling times of 0.1 and 0.5 ps, respectively, are used. A cutoff scheme where the short-ranged LJ interactions are computed only when the distance between two groups is less than 1 nm is used. During the simulations, the LJ parameters for unlike groups are evaluated by using the following mixing rule: $\sigma_{ij} = \sqrt{\sigma_i \sigma_j}$ and $\epsilon_{ij} = \sqrt{\epsilon_i \epsilon_j}$. All electrostatic interactions are calculated using the Particle Mesh Ewald technique,⁹⁷ where a real space cutoff of 0.9 nm and a Fourier spacing of 0.12 nm are used. A time-step of 2 fs is used in all the simulations and the trajectories are saved every 2 ps. Typically, the simulations are carried for 15 ns, and the last 10 ns are used for analysis. It is possible that the complexes do not attain their equilibrium configurations during the course of the simulation.

Table 2. Charge Assignment and Force-Field Parameters for the PAA Chain

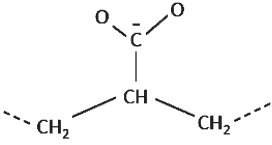
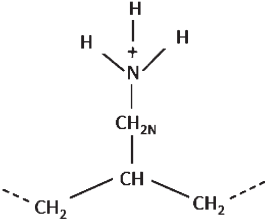
		Non-bonded interactions			
		Group	Charge (e)	σ (Å)	ϵ (kJ/mol)
		CH ₃	0	3.79	0.7530
		CH ₂	0	3.95	0.5856
		CH	0	4.23	0.5441
		C	0.84	3.76	0.1574
		O	-0.92	2.76	0.7731
		Bonded interactions			
		Bond	Length (Å)	Angle	K_θ (kJ/mol-rad ²) θ_0 (deg)
		CH ₂ -CH	1.53	CH ₂ -CH-CH ₂	460 109.5
		CH-C	1.53	CH ₂ -CH-C	504 110
		C-O	1.23	CH-C-O	504 118
				O-C-O	1008 124
Torsional potential					
Ryckaert-Bellmans [80]		proper torsional potential (cf. Eq. (6))			
CH ₂ -CH-CH ₂ -CH(kJ/mol)			CH-CH ₂ -CH-C	CH ₂ -CH-C-O	
$C_0 = 8.397$	$C_1 = 16.785$	k_{proper} (kJ/mol)	5.8576	0.4184	
$C_2 = 1.134$	$C_3 = -26.316$	ϕ_0 (deg)	0	0	
$C_4 = 0$	$C_5 = 0$	n	3	6	

Table 3. Charge Assignment and Force-Field Parameters for the PAH Chain

		Non-bonded interactions			
		Group	Charge (e)	σ (Å)	ϵ (kJ/mol)
		CH ₃	0	3.79	0.7530
		CH ₂	0	3.95	0.5856
		CH	0	4.23	0.5441
		CH _{2N}	0.31	3.95	0.5856
		N	-0.30	3.25	0.7140
		H	0.33	0	0
		Bonded interactions			
		Bond	Length (Å)	Angle	K_θ (kJ/mol-rad ²) θ_0 (deg)
		CH ₂ -CH	1.53	CH ₂ -CH-CH ₂	460 109.5
		CH-CH _{2N}	1.53	CH ₂ -CH-CH _{2N}	460 109.5
		CH _{2N} -N	1.47	CH-CH _{2N} -N	460 109.5
		N-H	1	CH _{2N} -N-H	377 109.5
				H-N-H	335 109.5
Torsional potential					
Ryckaert-Bellmans [80]		proper torsional potential (cf. Eq. (6))			
CH-CH ₂ -CH-CH _{2N} (kJ/mol)			CH ₂ -CH-CH _{2N} -N	CH-CH _{2N} -N-H	
$C_0 = 8.397$	$C_1 = 16.785$	k_{proper} (kJ/mol)	3.766	1.8830	
$C_2 = 1.134$	$C_3 = -26.316$	ϕ_0 (deg)	0	0	
$C_4 = 0$	$C_5 = 0$	n	3	3	

However, close agreement between implicit- (see section 4), where the system dynamics evolves faster due to reduced resistance in the absence of solvent, and explicit-solvent simulations, in most of the cases, suggests that detailed dynamics has a very weak influence on the structure of the complexes.

3. Results and Discussion: Explicit Solvent

As mentioned in section 1, we study PSS/PAH and PAA/PAH complex formation to understand the reasons behind the difference in the growth behavior of these films. Figure 1 shows snapshots of the two complexes. Each complex consists of five 20-mer polycations and five 20-mer polyanions, and is immersed in a solvent (water) bath. A more quantitative description of the structural and compositional properties of the complexes will be given next.

3.1. Properties of PAA/PAH and PSS/PAH Complexes.

We investigated the effect of the number of monomers, N_m (chain size), on the structural and compositional properties of the complexes. In doing so, the number of water molecules included was chosen to keep the system density approximately the same in all the cases. For $N_m = 10, 20, 30, 40$, and 50 , we included 5000, 8000, 9000, 10000, and 12000 water molecules, respectively, which result in system densities of approximately 0.93 and 0.89 g/cm^3 for PAA/PAH and PSS/PAH complexes, respectively. For $N_m = 20$, this yields polyelectrolyte concentration of 6×10^{-4} and $6.5 \times 10^{-4} \text{ M}$ (in monomer units) for PAA/PAH and PSS/PAH complexes, respectively. We also performed simulations with a different number of water molecules; for 20-mer chains, the number of water molecules was changed from 8000 to 5000. Because the simulations were performed under a constant pressure condition, decreasing the number of water molecules decreases the size of the simulation box, resulting in polyelectrolyte concentration of 9×10^{-4} and $1 \times 10^{-3} \text{ M}$ for PAA/PAH and PSS/PAH complexes, respectively. We found that this change in polyelectrolyte concentration has a very small effect on the structural properties of the two complexes. For a polyelectrolyte concentration of 6×10^{-4} and $9 \times 10^{-4} \text{ M}$, the radius of gyration of a PSS/PAH complex is 1.88 and 1.91 nm , respectively, and the radius of gyration of a PAA/PAH complex for polyelectrolyte concentration of 6.5×10^{-4} and $1 \times 10^{-3} \text{ M}$ is 1.68 and 1.71 nm , respectively.

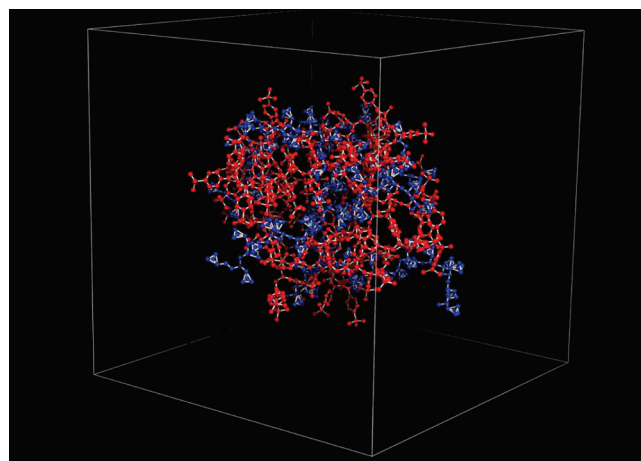
For all values of N_m , a net neutral spherical complex is formed consistent with a theoretical prediction of Zhang and Shklovskii.⁹⁸ Figure 2 shows the variation in swelling ratio, δ , which is the ratio of the radius-of-gyration of the complex to the radius-of-gyration of the corresponding single polyanion, with N_m . The swelling ratio is an effective way to compare the size of complexes made from different polyanions as the size of the polyanions gets scaled out. Here and elsewhere, error in the properties was calculated in the following way:⁹⁹

$$\Delta(A) = \sqrt{\frac{\sigma^2}{N_{\text{sig}}}} \quad (7)$$

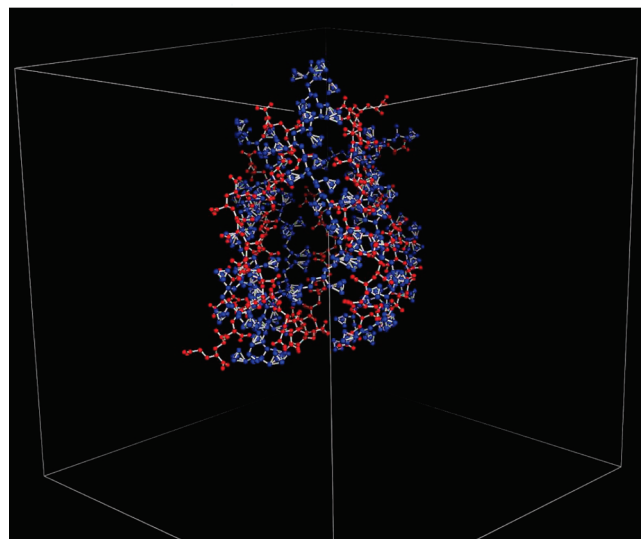
where $\Delta(A)$ is the error in property A and σ^2 is the variance. The number of statistically significant points, $N_{\text{sig}} = \tau_{\text{run}}/\tau_A$, where τ_{run} is the duration of simulation run. The correlation time, τ_A , is obtained by fitting the autocorrelation function of property A , $C_{AA}(t)$, versus time with an exponential decay:

$$C_{AA}(t) = C_{AA}(0) \exp(-t/\tau_A) \quad (8)$$

For both the complexes, δ decreases with increasing N_m . Presumably, at small N_m , the chains are more rigid over a



(a)



(b)

Figure 1. Snapshots showing (a) PSS/PAH and (b) PAA/PAH complexes. The simulation box contains five 20-mer polycations and five 20-mer polyanions, and 8000 water molecules (not shown). The polyanions are shown in orange and the PAH chains in blue.

large fraction of their length, and hence, the complex formed is more extended. As N_m increases, a more compact complex is formed due to a decrease in chain rigidity relative to the chain length. The more striking finding is that the PAA/PAH complex is around 25% more swollen than the PSS/PAH complex. This is consistent with an experimental finding that the amine group binds more strongly to the sulfonate group than to the carboxyl group,⁶⁵ resulting in a more compact complex.

The number of water molecules in the complex, N_w^c , is evaluated in the following way:

$$N_w^c = \int_0^{R_g^c} \rho(r) 4\pi r^2 dr \quad (9)$$

where R_g^c is the radius-of-gyration of the complex and $\rho(r)$ is the number density of water measured from the center-of-mass of the complex. From this, we determined the average number density of water molecules present in the complex:

$$\rho_w^c = \frac{3N_w^c}{4\pi(R_g^c)^3} \quad (10)$$

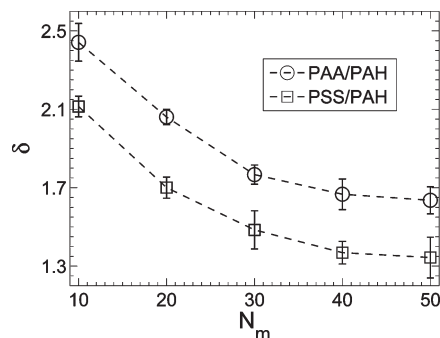


Figure 2. Variation in swelling ratio δ with chain length N_m for PAA/PAH and PSS/PAH complexes.

and the weight fraction of polyelectrolytes in the complex:

$$\phi_p = \frac{5(M^{pa} + M^{pc})}{5(M^{pa} + M^{pc}) + N_w^c M^w} \quad (11)$$

where the molecular weights of polyanion, polycation, and water are denoted by M^{pa} , M^{pc} , and M^w , respectively. Figure 3a,b show the variation in ρ_w^c and ϕ_p with N_m for the two complexes. Clearly, with an increase in N_m , ρ_w^c increases and ϕ_p decreases, suggesting that complexes formed by larger sized polyelectrolytes have a higher water content. This is due to the fact that complexes have fractal configurations. At a fixed N_m value, ρ_w^c is higher and ϕ_p is lower for the PAA/PAH complex, reinforcing the earlier finding that the PAA/PAH complex is more swollen. We also looked at the distribution of water molecules in the complex (not shown). In all the cases, we found that the inner core of the complex has a higher weight fraction of polyelectrolytes, and the weight fraction decreases with radial position. Even for LbL films it has been reported that the innermost layers are denser, while the outer layers are more solvated and less dense^{45,50}. Many experimental findings support the claim that during the deposition process the LbL film can be partitioned into three different zones: a precursor zone, a core zone, and an outer zone. The precursor zone is the region close to the substrate, the outer zone is the region close to the film surface, and the core zone is sandwiched between these two regions. Though, one notable difference in the case of polyelectrolyte complex is the absence of precursor zone because there is no substrate.

Next, we try to determine the reasons for the difference in the swelling behavior of the two complexes. Figure 4 shows the distribution of water molecules around the side groups of the two polyanions. The first plot shows the radial distribution function (RDF) between the PSS(PAA)–oxygen and the water–hydrogen. Clearly, the RDF for the PAA/PAH complex is more structured. For the PAA/PAH complex two peaks, one at 0.16 and the other at 0.30 nm, are observed, while for the PSS/PAH complex, a single peak in the RDF, at 0.18 nm, is observed. Also, the peaks are more pronounced for the PAA/PAH complex. Similar trends are observed even in the RDF between the PSS–sulfur (carboxylate–carbon in PAA) and the water–oxygen (see Figure 4b). There are more peaks in the RDF for the PAA/PAH complex and the peaks are more pronounced. Furthermore, in both the RDFs the peaks are observed at a smaller r for the PAA/PAH complex. Two conclusions can be drawn from the above findings. First, the water molecules associate more strongly with the carboxylic group than the sulfonate group. Second, the water molecules have a relatively long-ranged order around the PAA chain. The relatively higher affinity of water for the PAA chain (carboxylic group) gives a possible explanation for the relatively higher swelling for the PAA/PAH complex.

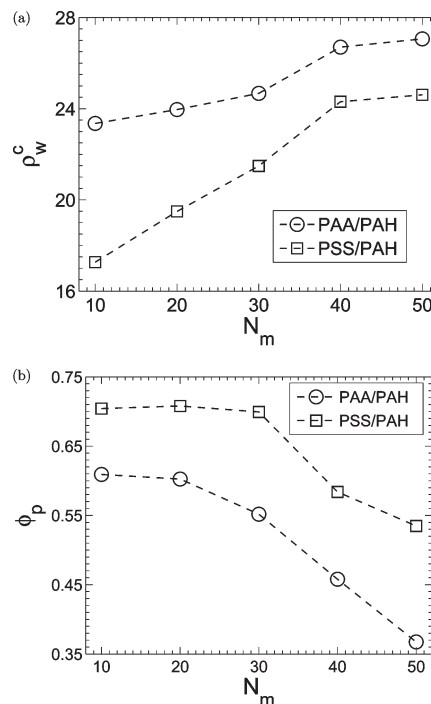


Figure 3. Variations in (a) the average number density of water molecules present in the complex, ρ_w^c , and (b) the weight fraction of polyelectrolytes in the complex, ϕ_p , with N_m for PAA/PAH and PSS/PAH complexes.

Another potential reason for the difference in the swelling behavior of the two complexes could be the difference in the chemical structure between the two polyanions. To test this hypothesis, we made the chemical structure of the PSS chain similar to that of the PAA chain. The phenyl rings were removed from the side groups of the PSS chain and the charged sulfonate groups were directly attached to the aliphatic backbone. We found that the complex formed by the modified-PSS and PAH chains swells more than does the normal PSS/PAH complex. In the two cases, respectively, $\delta = 2.26$ and 1.85 when $N_m = 20$, and $\delta = 1.90$ and 1.52 when $N_m = 40$. This suggests that the presence of a phenyl ring in the side group leads to the formation of a strongly bound complex. Presumably, the PSS chain can associate more easily with multiple oppositely charged polyelectrolytes because it has a bigger side group, and hence a more strongly bound complex is formed. It is also possible that due to the hydrophobic nature of the phenyl ring less water molecules are present in the complex, and as a consequence the resulting complex is more compact.

3.2. Parametric Study. Experimental studies have reported that salt concentration and pH have a profound effect on the properties of polyelectrolyte complexes.^{38,100} Additionally, the growth behavior and, as a consequence, the properties of LbL films, are strongly dependent on these factors^{54,57}. Hence, we next study the effects of these factors on the structure and composition of the two complexes.

3.2.1. Effect of Salt. Figure 5 shows the effect of KCl salt concentration (molarity, M) on the structural and compositional properties of PAA/PAH and PSS/PAH complexes. For both the complexes, swelling ratio increases with an increase in salt concentration. This is due to the weakening of electrostatic interactions caused by the screening of charges by salt ions. Hence, a weakly bound complex is formed at a higher M , and at a very high M , the complex dissociates. The above finding is in agreement with a similar increase in the

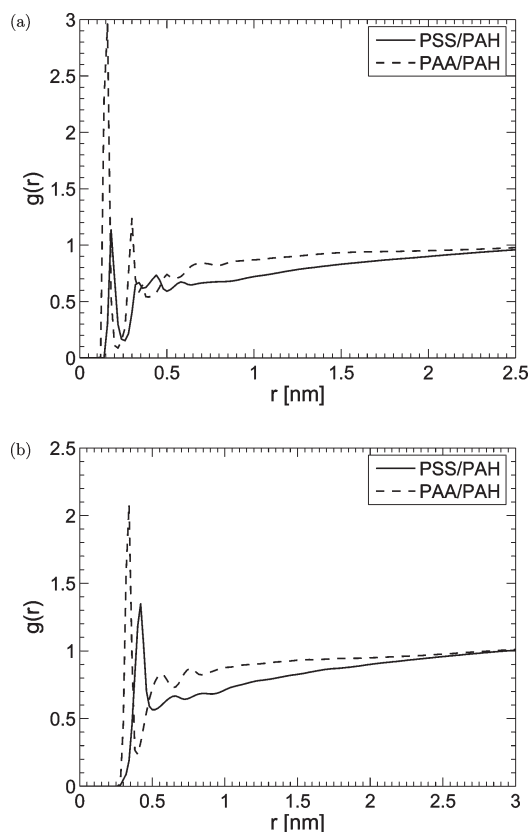


Figure 4. Radial distribution functions between: (a) the oxygen in PSS (PAA) and the hydrogen in water and (b) the sulfur (carbon) in PSS (PAA) and the oxygen in water. Note, the distance r is in nm.

thickness of PSS/PAH and PAA/PAH multilayer films with salt concentration.^{101,102} At a fixed M value, the PAA/PAH complex is more swollen than the PSS/PAH complex in agreement with a finding of section 3.1. However, by increasing the salt concentration, the PSS/PAH complex can be made to swell more than the PAA/PAH complex formed in the absence of salt.

Figure 5b shows that the weight fraction of polyelectrolytes, ϕ_p , decreases with M for both the complexes. Hence, it is expected that the diffusivity of polyelectrolytes through the complex, which increases with decreasing ϕ_p , will increase with increasing M . Because our one-dimensional LbL model presented elsewhere⁶⁹ predicts that exponential growth results from higher diffusion rates, the above finding gives a possible explanation for the change in the growth behavior of LbL films, from linear to exponential, with increasing salt concentration as reported in many previous studies.⁵⁴ In summary, adding salt increases the diffusivity of polyelectrolytes through LbL films, hence, the tendency of LbL films to grow exponentially increases. Figure 6 shows the weight fractions of potassium and chloride ions in the complexes. For both the complexes, the weight fraction increases approximately linearly with increasing M , which is indicative of an ideal phase behavior. Another point worth mentioning is that the concentration of salt ions in bulk is higher than in the complex. For the PSS/PAH complex, the partition coefficient, which is defined as the ratio of concentration in the bulk to that in the complex, is around 2.4 for the potassium ion and 2.2 for the chloride ion. For the PAA/PAH complex, the partition coefficient is around 1.4 for both the ions.

Figure 7 shows the RDFs between the oxygen in water and salt ions for the PSS/PAH complex; the distributions are identical for the PAA/PAH complex and for other salt

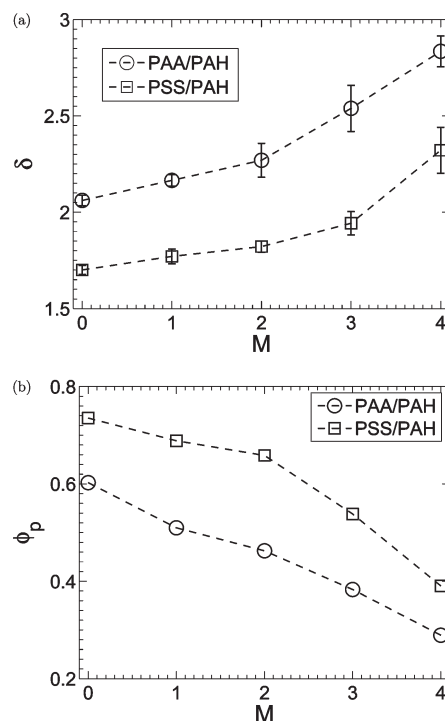


Figure 5. Variations in (a) swelling ratio δ and (b) the weight fraction of polyelectrolytes in the complex, ϕ_p , with KCl salt concentration, in molarity, M for PAA/PAH and PSS/PAH complexes when $N_m = 20$.

concentrations. It is clear from the plots that water molecules are distributed in an orderly manner around the two ions, suggesting that a hydration shell is present; the finding is consistent with the fact that the salt ions are hydrophilic. We also looked at the distribution of salt ions in the complex (not shown). For both the complexes, the salt ions reside primarily in solution or near the periphery of the complex. As discussed in the previous section, the inner core of both the complexes have a low water concentration, and the concentration first increases radially and then plateaus in the region away from the complex. The hydrophilic salt ions therefore prefer to remain in the vicinity of water molecules. A similar localization of salt ions in water-rich zones has also been reported in the case of PAA/PAH multilayer films.¹⁰³ Tanchak et al. used neutron reflectometry to determine the distribution of salt ions and water molecules in PAA/PAH films assembled in the presence of NaCl salt. They found that both water molecules and salt ions accumulate either near the substrate or near the film surface.

3.2.2. Effect of Charge Fraction. Because PSS is a strong acid (degree of ionization is 1), we only study the effect of variation in the degree of ionization of the PAA chain. Although we were not able to probe the effect of variation in the degree of ionization of the PAH chain due to shortage of computational resources, the qualitative trends are expected to be similar to the ones observed when the degree of ionization of the PAA chain is varied. Figure 8 shows the effect of the degree of ionization of the PAA chain, f . In the simulations, an appropriate number of chloride ions is added to ensure that the system remains electrostatically neutral. Figure 8a shows that the radius-of-gyration of the complex, R_g^c , has a minimum with respect to f , which indicates that the intermolecular attraction of unlike charges competes with the intramolecular repulsion of like charges on the same chain. For $f < 0.5$, intermolecular electrostatic attraction dominates, while for $f > 0.5$, the increasing proximity of like charges on the same chain causes intramolecular

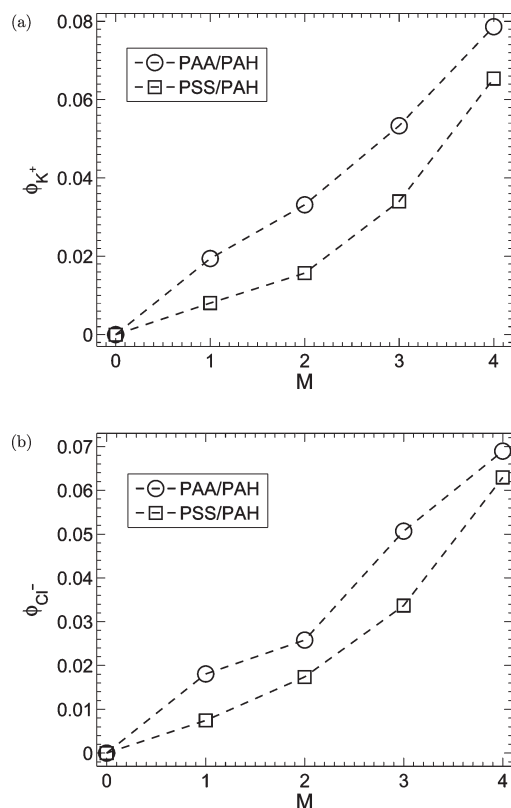


Figure 6. Variations in the weight fractions of (a) potassium and (b) chloride ions in the complex with M for PAA/PAH and PSS/PAH complexes when $N_m = 20$.

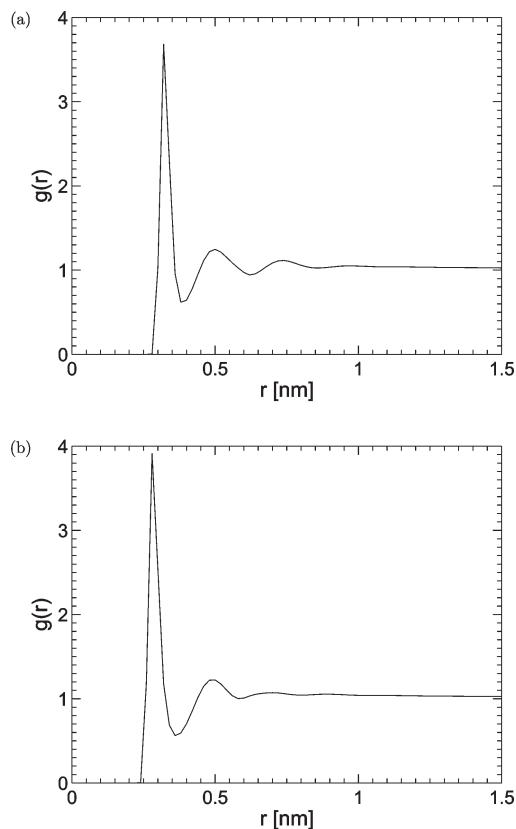


Figure 7. Radial distribution functions between the oxygen in water, and (a) chloride ion and (b) potassium ion, for the PSS/PAH complex. The concentration of KCl salt is 1 M and $N_m = 20$.

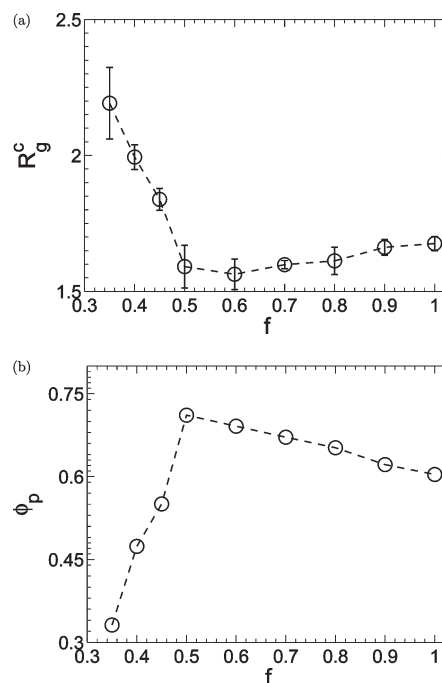


Figure 8. Variations in (a) the radius-of-gyration of the complex, R_g^c , and (b) polyelectrolyte weight fraction, ϕ_p , with the degree of ionization of the PAA chain, f , when $N_m = 20$ and $M = 0$.

electrostatic repulsion to dominate, and hence, R_g^c increases with increasing f . Figure 8b shows the variation in ϕ_p with f . The nonmonotonic dependence of ϕ_p on f reflects the trend seen in Figure 8a, and is in qualitative agreement with a prior experimental finding.¹⁰⁰ Gardlund et al. studied the formation of PAA/PAH complexes using static light scattering and found that the weight fraction of water (which should be roughly $1 - \phi_p$, that is, complementary to the weight fraction of polyelectrolytes) in the complex shows a minimum with respect to f . As is the case with salt ions, the counterions (chloride ions) are present either near the periphery of the complex or in the bulk. On the basis of the above results, a qualitative estimate of the effect of f on the diffusivity of polyelectrolytes through PAA/PAH complexes can eventually be made.

4. Implicit Solvent

Computational limitations restrict explicit-solvent, atomistic simulation to small system sizes and times of, at most, tens of nanoseconds. Previous studies suggest that the diffusivity of polyelectrolytes in the LbL film is one of the most important parameters that affects the assembly process. Both experimental predictions and order of magnitude estimates suggest that the diffusivity of polyelectrolytes through LbL films is very small (10^{-11} cm²/s).⁶⁹ To obtain a reasonable estimate of the diffusivity, simulations should be carried out for a much longer time (hundreds of nanoseconds). One possible way to overcome these computational limitations is to perform implicit-solvent, atomistic simulations. Exclusion of solvent hydrodynamic interaction (HI) is expected to have only a small effect on the dynamics because in the semidilute regime, which is of interest, HI has a very small effect on the dynamics.^{104,105} Also, simulations performed on larger systems will allow us to validate the findings of the explicit-solvent simulations performed for smaller system sizes.

The main challenge with the implicit-solvent simulation is the development of a force field that can accurately capture the

features of the explicit-solvent simulation. To address this, we have developed a new coarse-graining strategy. In this strategy, the electrostatic and nonelectrostatic interaction parameters are tuned such that the radius-of-gyration of the complex and the intermolecular radial distribution functions between various charged groups predicted by the implicit-solvent simulation match those predicted by the explicit-solvent simulation. The parameters for the attractive part of the LJ potential, $C6_i^{\text{Imp}}$, for the implicit-solvent simulation are obtained using

$$C6_i^{\text{Imp}} = (\sqrt{C6_i} - \gamma_j \sqrt{C6_w})^2 \quad (12)$$

where $C6_i$ and $C6_w$ are the parameters for the attractive part of the LJ potential for component i and water, and γ_j is the tunable parameter for the j th molecule. The above equation accounts for the screening of LJ attractions due to the presence of solvent, that is, water in this case. This relationship is similar to the one used to account for the screening of van der Waals attraction (Hamaker constant) between two macroscopic bodies because of the presence of a medium.¹⁰⁶ Another factor that needs to be accounted for is the screening of electrostatic interactions due to the presence of solvent. For the simple case in which the solvent is uniformly distributed, the screening of electrostatic interactions can be accurately accounted for by using a uniform dielectric permittivity different than 1 (note that a value of 79 is used in bulk water). However, the case of complex formation is more subtle because the dielectric permittivity is not uniform. In general, there are three regions: (i) the region where polycations and polyanions bind with each other, which is depleted in water, (ii) the region of bulk water, and (iii) the region of intermediate water concentration. To include this effect in a simple manner, we calculate the electrostatic energy, U_{elec} , in the following way:

$$U_{\text{elec}}(r_{ij}) = \frac{q_i q_j}{4\pi\epsilon_0 \epsilon_r(r_{ij}) r_{ij}} \quad (13)$$

where ϵ_0 is the dielectric constant, q_i and q_j are the charges carried by the i th and j th groups, and r_{ij} is the distance between the two groups. We use the following functional form for the dielectric permittivity, $\epsilon_r(r)$:

$$\epsilon_r(r) = \begin{cases} \epsilon^{\text{near}} & r < r_c \\ \epsilon^{\text{bulk}} & r > r_c \end{cases} \quad (14)$$

where ϵ^{bulk} is the dielectric permittivity in the bulk, and r_c and ϵ^{near} are two tuning parameters. When $r \geq r_c$, the electrostatic interaction between two charged groups is evaluated assuming that the groups are present in bulk solvent, and when $r < r_c$, the electrostatic interaction is evaluated assuming that the concentration of solvent in the region between the two charged groups is less than its bulk value. A similar methodology was used by Jusufi et al. to account for electrostatic interactions in the implicit-solvent simulation of micelle formation.¹⁰⁷ In the expression for electrostatic energy (viz., eq 13), the contribution due to image charges¹⁰⁴ has been neglected. For dilute and semidilute polyelectrolyte solutions, this contribution is expected to be small as the image charges would be located significant distances away from the real charges, while for concentrated polyelectrolyte solutions, a uniform dielectric permittivity will be adequate to accurately describe the electrostatic interactions. However, the contribution due to image charges should be included when the concentration lies in between semidilute and concentrated regimes.

For the implicit-solvent simulation, the GROMACS source code was accordingly modified to account for the variation in dielectric permittivity with distance. By following the above

Table 4. Implicit-Solvent Tuning Parameters

parameter	PAA/PAH	PSS/PAH
γ_{PAH}	0.33	0.50
$\gamma_{\text{PAA(PSS)}}$	0.10	0.04
ϵ^{near}	1.80	1.50
r_c (nm)	0.23	0.25

strategy, we developed implicit-solvent force fields for both PAA/PAH and PSS/PAH systems. Table 4 lists the tuning parameters used for the two complexes. The implicit-solvent simulation was performed under isothermal-isochoric (NVT) conditions, and we used the same box size as that used in the explicit-solvent simulation.

The radial distribution functions predicted by the explicit- and implicit-solvent simulations for the two complexes when $N_m = 20$ are shown in Figures 9 and 10. For the PAA/PAH complex, both explicit- and implicit-solvent simulations predict two maxima in the RDF between the carboxyl-carbon and the amine-nitrogen, located at 0.34 and 0.60 nm. The first peak in the RDF arises due to the interaction between the carboxyl group with the amine group, while the second peak arises due to the interaction between the carboxyl group with the neighboring amine groups. Even the RDF between the carboxyl-oxygen and the amine-hydrogen is well-structured with peaks at 0.15, 0.29, and 0.50 nm. It is clear from the plots that the RDFs predicted by the explicit- and implicit-solvent simulations coincide. Also, the radius-of-gyration of the PAA/PAH complex predicted by the implicit-solvent simulation (1.68 ± 0.02 nm) matches well with that predicted by the explicit-solvent simulation (1.68 ± 0.03 nm).

Figure 10 shows the RDFs, predicted by the implicit- and explicit-solvent simulations, for the PSS/PAH complex. The strong interaction between the sulfonate and the amine groups is reflected in the well-structured RDFs. Both explicit- and implicit-solvent simulations predict that there is a maximum in the RDF between the sulfonate-sulfur and the amine-nitrogen, which is located at 0.43 nm, and there are four maxima in the RDF between the sulfonate-oxygen and the amine-hydrogen, which are located at 0.18, 0.32, 0.44, and 0.55 nm. The RDFs predicted by both the simulation methods almost overlap, except that in the RDF between the sulfonate-sulfur and the amine-nitrogen, the peak predicted by the implicit-solvent simulation is less pronounced than that predicted by the explicit-solvent simulation. Additionally, the R_g value predicted by the implicit-solvent simulation (1.92 ± 0.03) closely matches with the value predicted by the explicit-solvent simulation (1.88 ± 0.02). The close agreement between the predictions of the explicit- and implicit-solvent simulations for both PAA/PAH and PSS/PAH complexes suggests that the proposed coarse-graining strategy captures extremely well both near- and far-field aspects of complex formation. Furthermore, a significant computational speed-up was obtained with the implicit-solvent simulation. For example, the average computational speeds were 0.16 and 1 ns/day, respectively, for the explicit- and implicit-solvent simulations of complex formation between five chains each of 20-mer PAA and PAH. The speed-up is even more significant for bigger system sizes when the explicit-solvent simulation is much slower due to the presence of a large number of solvent molecules.

We then performed implicit-solvent simulations to compare with other predictions of explicit-solvent simulations, and to ensure that these findings hold even for larger system sizes. Figure 11 shows the effect of N_m on R_g^c for both the complexes, and as expected, R_g^c increases with N_m . For $N_m \leq 50$, the radii-of-gyration predicted by the implicit-solvent simulation match with the explicit-solvent simulation predictions for both complexes, except for the slight discrepancy between the two predictions when $N_m = 50$. Presumably, for $N_m = 50$, the complexes did not achieve their equilibrium configurations during the short course

of the explicit-solvent simulation. We also studied the variation in swelling ratio δ with N_m (results not shown). As predicted for $N_m \leq 50$, we found that the PAA/PAH complex is more swollen

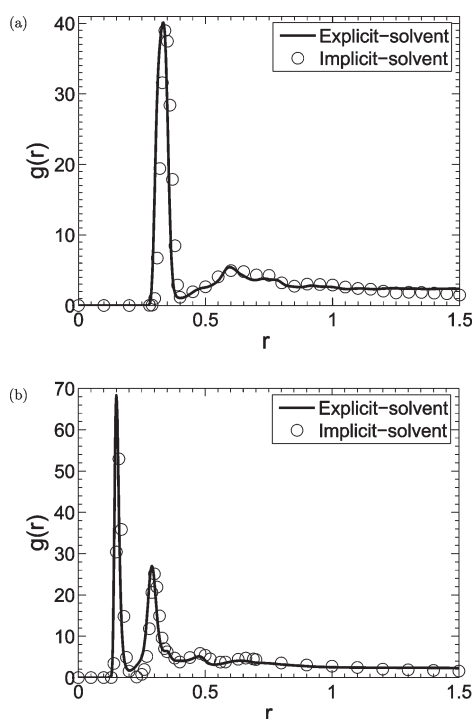


Figure 9. Radial distribution functions between (a) the carboxyl-carbon and the amine-nitrogen and (b) the carboxyl-oxygen and the amine-hydrogen for the PAA/PAH complex when $N_m = 20$.

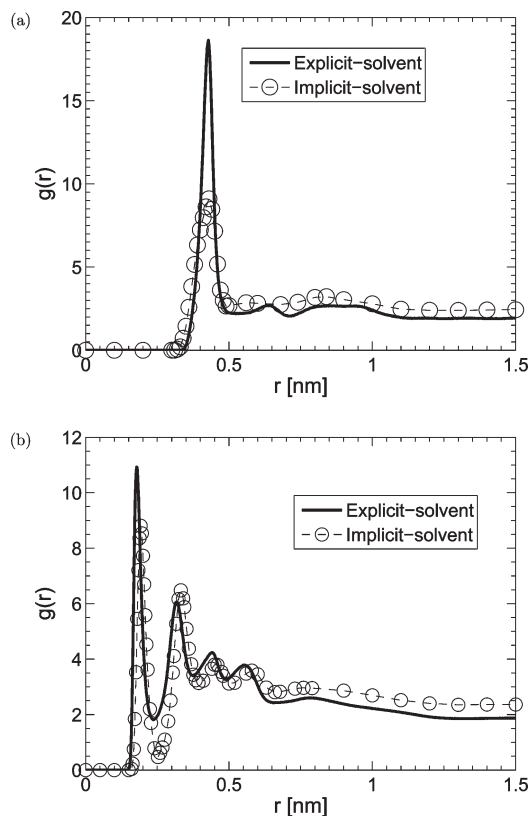


Figure 10. Radial distribution functions between (a) the sulfonate-sulfur and the amine-nitrogen and (b) the sulfonate-oxygen and the amine-hydrogen for the PSS/PAH complex when $N_m = 20$.

than the PSS/PAH complex even when $N_m > 50$. The swelling ratios for PSS/PAH and PAA/PAH complexes are 1.15 and 1.40, respectively, when $N_m = 100$.

The implicit-solvent simulation was further extended to study the effect of salt. The explicit-solvent simulation predicts that a hydration shell is present around the two salt ions (see section 3.2.1). To take this into account, the parameters for the repulsive part of LJ interaction, C_{12} , of salt ions, which physically correspond to the size of the salt ions, was tuned. Figure 12 shows the variation in R_g^c with KCl salt concentration, M , for both complexes. Note, the parameters C_{12} for the salt ions used in the implicit-solvent simulation have twice the values used in the explicit-solvent simulation. The predictions of the two simulations are in reasonable agreement with a better match observed for the PSS/PAH complex. Because the radius of the hydration shell depends on molarity M , a much better agreement can be obtained by making the parameter C_{12} vary with M . Nevertheless, the above strategy is a simple way to account for the presence of the hydration shell and it works reasonably well. Figure 13 shows the effect of the degree of ionization of the PAA chain, f , on the radius-of-gyration of the PAA/PAH complex. The prediction of the implicit- and explicit-solvent simulations does not completely match: the implicit-solvent simulation predicts that R_g^c monotonically decreases with increasing f , which is in contrast to the nonmonotonic dependence predicted by the explicit-solvent simulation. This mismatch could be due to the fact that at intermediate f values the two-parameter functional form (cf. eq 14) used to describe the variation in the dielectric permittivity with distance is not a good description. A similar mismatch between implicit- and explicit-solvent simulations was observed in the all-atom simulations performed by Ju et al.,¹⁰⁸ to study the behavior of single poly(methacrylic acid) in aqueous

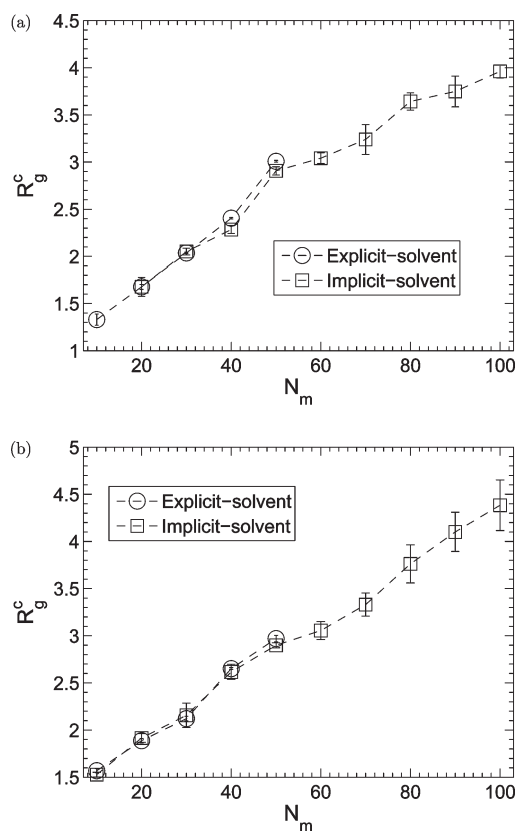


Figure 11. Comparisons between the predictions of explicit- and implicit-solvent simulations for (a) PAA/PAH and (b) PSS/PAH complexes. Variation in R_g^c with N_m when $M = 0$ and $f = 1$.

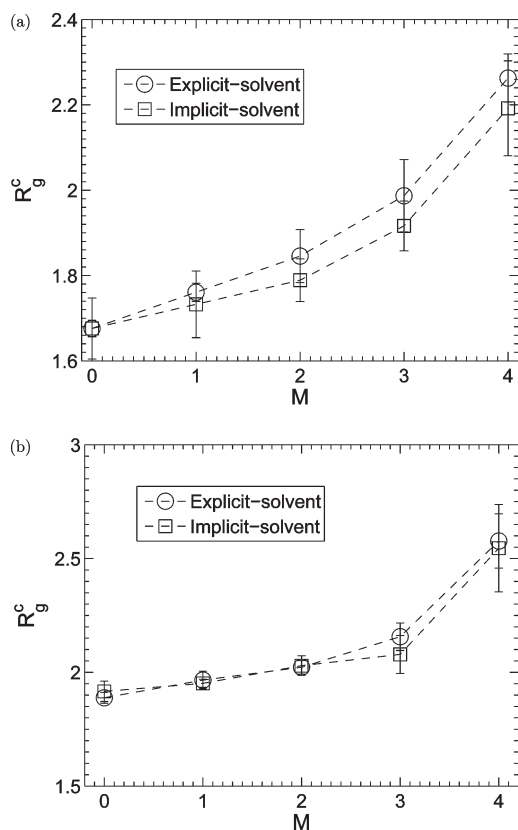


Figure 12. Comparisons between the predictions of explicit- and implicit-solvent simulations for (a) PAA/PAH and (b) PSS/PAH complexes. Variation in R_g^c with salt molarity M when $N_m = 20$ and $f = 1$.

solution. However, in their study, the implicit-solvent simulation underpredicted the radius-of-gyration at intermediate charge fractions.

5. Conclusions

We have studied the formation of PSS/PAH and PAA/PAH complexes using explicit- and implicit-solvent, atomistic simulations. The choice of systems is motivated by the fact that, during LbL assembly, one of the systems, PAA/PAH, can exhibit exponential growth, while the other always grows linearly. The close connection between polyelectrolyte complexation and LbL assembly, as reported in prior studies, coupled with the computational limitations associated with the use of atomistic simulation to study LbL assembly, motivated us to study polyelectrolyte complexation. We used united-atom force fields to model polyelectrolytes, and the accuracy of the force-field parameters was checked by comparing with previous experimental and simulation results. In all our simulations, the polyelectrolytes have the same number of monomers and are present in stoichiometric proportion, and water is used as solvent. The simulations give important insights into the structure and composition of the polyelectrolyte complexes. We proposed a simple strategy to develop a force field for the implicit-solvent simulation. In the absence of salt and for fully charged polyelectrolytes, the radius-of-gyration as well as the various radial distribution functions predicted by the implicit-solvent simulation are in excellent agreement with the explicit-solvent simulation predictions, while reasonable agreement is obtained in the other cases. Both the simulation methods predict that the PSS/PAH complex is more compact and has a smaller fraction of water than the PAA/PAH complex. This appears to be due to the presence of phenyl rings in the PSS chain and the hydrophilic nature of the carboxylic group

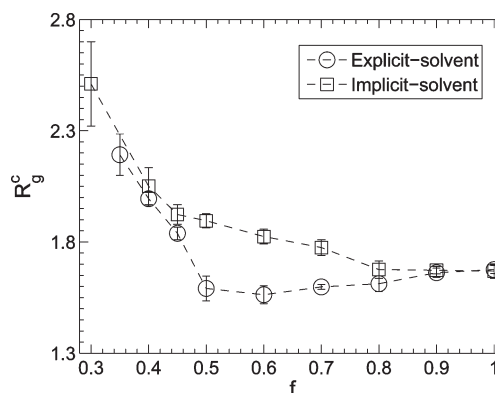


Figure 13. Comparison between explicit- and implicit-solvent simulations for the PAA/PAH complex: R_g^c vs the degree of ionization of the PAA chain f when $N_m = 20$.

in the PAA chain. Furthermore, we studied complex formation between polyelectrolyte chains with more monomers ($N_m > 50$) using the implicit-solvent simulation. We found that the prediction that the PAA/PAH complex is more swollen than the PSS/PAH complex holds even for longer polyelectrolytes, suggesting that our findings are independent of chain size. The simulations also predict that an increase in salt concentration or a decrease in partial charge fraction increases swelling and the weight fraction of water in the complex, in accord with prior experimental studies. On the basis of the above results, a qualitative estimate of the effects of salt concentration and charge fraction on the diffusivity of polyelectrolytes through the two complexes can be made.

Previous experimental and analytical studies⁶⁹ suggest that the diffusivity of “free” polyelectrolytes in LbL film is one of the most important parameters influencing its growth behavior. The implicit-solvent simulation can be used to estimate the diffusivity of a “free” polyelectrolyte in a complex and will be a subject of future investigation. Furthermore, the effects of assembly conditions, such as pH and salt, on diffusivity can also be probed. Despite the fact that atomistic simulation provide crucial information about LbL assembly, additional levels of coarse-graining that will allow us to perform longer time simulations will be needed to develop a quantitative understanding about it. Future studies should try to develop efficient strategies to map atomistic polyelectrolyte chains to coarse-grained bead-rod chains so that the details of the structure of the polyelectrolyte chains get accurately transferred. Once such a coarse-graining is successfully performed, the entire LbL process can be accurately simulated. In summary, the simulation of LbL assembly is challenging, but we think a systematic coarse-graining approach along the lines of the one proposed here will allow us to successfully tackle this problem.

References and Notes

- (1) Durstock, M. F.; Taylor, B.; Spry, R. J.; Chiang, L.; Reulbach, S.; Heitfeld, K.; Baur, J. W. *Synth. Met.* **2001**, *116*, 373–377.
- (2) Durstock, M. F.; Spry, R. J.; Baur, J. W.; Taylor, B. E.; Chiang, L. Y. *J. Appl. Phys.* **2003**, *94*, 3253–3259.
- (3) Li, H.; Li, Y.; Zhai, J.; Cui, G.; Liu, H.; Xiao, S.; Liu, Y.; Lu, F.; Jiang, L.; Zhu, D. *Chem.—Eur. J.* **2003**, *9*, 6031–6038.
- (4) Hasobe, T.; Kamat, P. V.; Absalom, M. A.; Kashiwagi, Y.; Sly, J.; Crossley, M. J.; Hosomizu, K.; Imahori, H.; Fukuzumi, S. *J. Phys. Chem. B* **2004**, *108*, 12865–12872.
- (5) Pradhan, B.; Bandhyopadhyay, A.; Pal, A. J. *Appl. Phys. Lett.* **2004**, *85*, 663–665.
- (6) Lowman, G. M.; Hammond, P. T. *Small* **2005**, *1*, 1070–1073.
- (7) Liang, Z.; Dzienis, K. L.; Xu, J.; Wang, Q. *Adv. Funct. Mater.* **2006**, *16*, 542–548.
- (8) Man, K. Y. K.; Wong, H. L.; Chan, W. K.; Kwong, C. Y.; Djuricic, A. B. *Chem. Mater.* **2004**, *16*, 365–367.

- (9) Man, K. Y. K.; Wong, H. L.; Chan, W. K.; Djuricic, A. B.; Beach, E.; Rozeveld, S. *Langmuir* **2006**, *22*, 3368–3375.
- (10) Mwaura, J. K.; Pinto, M. R.; Witker, D.; Ananthakrishnan, N.; Schanze, K. S.; Reunolds, J. R. *Langmuir* **2005**, *21*, 10119–10126.
- (11) Saab, M. A.; Abdel-Malak, R.; Wishart, J. F.; Ghaddar, T. H. *Langmuir* **2007**, *23*, 10807–10815.
- (12) Wang, S.; Li, C.; Chen, F.; Shi, G. *Nanotechnology* **2007**, *18*, 185707.
- (13) Farhat, T. R.; Hammond, P. T. *Adv. Funct. Mater.* **2005**, *15*, 945–954.
- (14) Jiang, S. P.; Liu, Z.; Tian, Z. Q. *Adv. Mater.* **2006**, *18*, 1068–1072.
- (15) Phillips, A. K.; Moore, R. B. *J. Polym. Sci., Part B: Polym. Phys.* **2006**, *44*, 2267–2277.
- (16) Xi, J.; Wu, Z.; Teng, X.; Zhao, Y.; Chen, L.; Qiu, X. *J. Mater. Chem.* **2008**, *18*, 1232–1238.
- (17) Chluba, J.; Voegel, J.-C.; Decher, G.; Erbacher, P.; Schaaf, P.; Ogier, J. *Biomacromolecules* **2001**, *2*, 800–805.
- (18) Serizawa, T.; Yamaguchi, M.; Akashi, M. *Biomacromolecules* **2002**, *3*, 724–731.
- (19) Mendelsohn, J. D.; Yang, S. Y.; Hiller, J. A.; Hochbaum, A. I.; Rubner, M. F. *Biomacromolecules* **2003**, *4*, 96–106.
- (20) Izumrudov, V. A.; Kharlampieva, E.; Sukhishvili, S. A. *Biomacromolecules* **2005**, *6*, 1782–1788.
- (21) Lvov, Y.; Caruso, F. *Anal. Chem.* **2001**, *73*, 4212–4217.
- (22) Thierry, B.; Kujawa, P.; Tkaczyk, C.; Winnik, F. M.; Bilodeau, L.; Tabrizian, M. *J. Am. Chem. Soc.* **2005**, *127*, 1626–1627.
- (23) Benkirane-Jessel, N.; Atalar, F.; Laval, P.; Mutterer, J.; Decher, G.; Schaaf, P.; Voegel, J.-C.; Ogier, J. *Adv. Mater.* **2003**, *15*, 692–695.
- (24) Brynda, E.; Pachernik, J.; Houska, M.; Pientka, Z.; Dvorak, P. *Langmuir* **2005**, *21*, 7877–7883.
- (25) Benkirane-Jessel, N.; Laval, P.; Hubsch, E.; Holl, V.; Senger, B.; Haikel, Y.; Voegel, J.-C.; Ogier, J.; Schaaf, P. *Adv. Funct. Mater.* **2005**, *15*, 648–654.
- (26) Sun, Y.; Sun, C.; Wang, B.; Shen, J. *Macromol. Chem. Phys.* **1996**, *197*, 147–153.
- (27) Tang, Z.; Wang, Y.; Podsiadlo, P.; Kotov, N. A. *Adv. Mater.* **2006**, *18*, 3203–3224.
- (28) Burke, S. E.; Barrett, C. J. *Macromolecules* **2004**, *37*, 5375–5384.
- (29) Kharlampieva, E.; Ankner, J. F.; Rubinstein, M.; Sukhishvili, S. A. *Phys. Rev. Lett.* **2008**, *100*, 128303.
- (30) Srivastava, S.; Ball, V.; Podsiadlo, P.; Lee, J.; Ho, P.; Kotov, N. A. *J. Am. Chem. Soc.* **2008**, *130*, 3748–3749.
- (31) Szarpak, A.; Pignot-Paintrand, I.; Nicolas, C.; Picart, C.; Auzley-Velty, R. *Langmuir* **2008**, *24*, 9767–9774.
- (32) Podsiadlo, P.; Kaushik, A. K.; Arruda, E. M.; Waas, A. M.; Shim, B. S.; Xu, J.; Nandivata, H.; Pumphlin, B. G.; Lahann, J.; Ramamoorthy, A.; Kotov, N. A. *Science* **2007**, *318*, 80–83.
- (33) Decher, G.; Hong, J. D. *Thin Solid Films* **1992**, *210*, 831–835.
- (34) Decher, G. *Science* **1997**, *277*, 1232–1237.
- (35) Ou, Z.; Muthukumar, M. J. *Chem. Phys.* **2006**, *124*, 154902.
- (36) Bakeev, K. N.; Izumrudov, V. A.; Kuchanov, S. I.; Zezin, A. B.; Kabanov, V. A. *Macromolecules* **1992**, *25*, 4249–4254.
- (37) Kabanov, V. A. *Fundamentals of polyelectrolyte complexes in solution and bulk. In multilayer thin films*; Wiley: New York, 2003.
- (38) Dautzenberg, H. *Macromolecules* **1997**, *30*, 7810–7815.
- (39) Dautzenberg, H.; Karibyan, N. *Macromol. Chem. Phys.* **1999**, *200*, 118–125.
- (40) de Vries, R.; Stuart, M. C. *Curr. Opin. Colloid Interface Sci.* **2006**, *11*, 295–301.
- (41) Lee, J.; Popov, Y. O.; Fredrickson, G. H. *J. Chem. Phys.* **2008**, *128*, 224908.
- (42) Hayashi, Y.; Ulner, M.; Linse, P. *J. Chem. Phys.* **2002**, *116*, 6836–6845.
- (43) Hayashi, Y.; Ulner, M.; Linse, P. *J. Phys. Chem. B* **2003**, *107*, 8198–8207.
- (44) Hayashi, Y.; Ulner, M.; Linse, P. *J. Phys. Chem. B* **2004**, *108*, 15266–15277.
- (45) Ladam, G.; Schaaf, P.; Voegel, J.-C.; Schaaf, P.; Decher, G.; Cuisinier, F. *Langmuir* **2000**, *16*, 1249–1255.
- (46) Laval, P.; Gergely, C.; Cuisinier, F. J. G.; Decher, G.; Schaaf, P.; Voegel, J.-C.; Picart, C. *Macromolecules* **2002**, *35*, 4458–4465.
- (47) Picart, C.; Laval, P.; Hubert, P.; Cuisinier, F. J. G.; Decher, G.; Schaaf, P.; Voegel, J.-C. *Langmuir* **2001**, *17*, 7414–7424.
- (48) Picart, C.; Mutterer, J.; Richert, L.; Luo, Y.; Perstwich, G. D.; Schaaf, P.; Voegel, J.-C.; Laval, P. *Proc. Natl. Acad. Sci. U.S.A.* **2005**, *102*, 18321–18325.
- (49) Laval, P.; Vivet, V.; Jessel, N.; Decher, G.; Voegel, J.-C.; Mesini, P. J.; Schaaf, P. *Macromolecules* **2004**, *37*, 1159–1162.
- (50) Porcel, C.; Laval, P.; Ball, V.; Decher, G.; Senger, B.; Voegel, J.-C.; Schaaf, P. *Langmuir* **2006**, *22*, 4376–4383.
- (51) Haynie, D. T.; Balkundi, S.; Palath, N.; Chakravarthula, K.; Dave, K. *Langmuir* **2004**, *20*, 4540–4547.
- (52) Boulmedais, F.; Ball, V.; Schwint, P.; Frisch, B.; Schaaf, P.; Voegel, J.-C. *Langmuir* **2003**, *19*, 440–445.
- (53) Kujawa, P.; Moraille, P.; Sanchez, J.; Badia, A.; Winnik, F. M. *J. Am. Chem. Soc.* **2005**, *127*, 9224–9234.
- (54) Liu, G.; Zhao, J.; Sun, Q.; Zhang, G. *J. Phys. Chem. B* **2008**, *112*, 3333–3338.
- (55) Salomaki, M.; Laiho, T.; Kankare, J. *Macromolecules* **2004**, *37*, 9685–9590.
- (56) Salomaki, M.; Laiho, T.; Kankare, J. *Langmuir* **2004**, *20*, 3679–3683.
- (57) Schoeler, B.; Poptoshev, E.; Caruso, F. *Macromolecules* **2003**, *36*, 5258–5264.
- (58) Choi, J.; Rubner, M. F. *Macromolecules* **2005**, *38*, 116–124.
- (59) Itano, K.; Choi, J.; Rubner, M. F. *Macromolecules* **2005**, *38*, 3450–3460.
- (60) Fu, J.; Ji, J.; Shen, L.; Kuller, A.; Rosenhahn, A.; Shen, J.; Grunze, M. *Langmuir* **2009**, *25*, 672–675.
- (61) Elzbieciak, M.; Zapotoczny, S.; Nowak, P.; Krastev, R.; Nowakowska, M.; Warszynski, P. *Langmuir* **2009**, *25*, 3255–3259.
- (62) Tan, H. L.; Mcmurdo, M. J.; Pan, G.; Patten, P. G. V. *Langmuir* **2003**, *19*, 9311–9314.
- (63) Salomaki, M.; Vinokurov, I. A.; Kankare, J. *Langmuir* **2005**, *21*, 11232–11240.
- (64) Poptoshev, E.; Schoeler, B.; Caruso, F. *Langmuir* **2004**, *20*, 829–834.
- (65) Cho, J.; Quinn, J. F.; Caruso, F. *J. Am. Chem. Soc.* **2004**, *126*, 2270–2271.
- (66) Hubsch, E.; Ball, V.; Senger, B.; Decher, G.; Voegel, J.-C.; Schaaf, P. *Langmuir* **2004**, *20*, 1980–1985.
- (67) Porcel, C.; Laval, P.; Decher, G.; Senger, B.; Voegel, J.-C.; Schaaf, P. *Langmuir* **2007**, *23*, 1898–1904.
- (68) Sun, B.; Jewell, C. M.; Fredin, N. J.; Lynn, D. M. *Langmuir* **2007**, *23*, 8452–8459.
- (69) Hoda, N.; Larson, R. G. *J. Phys. Chem. B* **2009**, *113*, 4232–4241.
- (70) Messina, R. *Macromolecules* **2004**, *37*, 621–629.
- (71) Abu-Sharkh, B. *J. Chem. Phys.* **2005**, *123*, 114907.
- (72) Patel, P. A.; Jeon, J.; Mather, P. T.; Dobrynin, A. V. *Langmuir* **2005**, *21*, 6113–6122.
- (73) Patel, P. A.; Jeon, J.; Mather, P. T.; Dobrynin, A. V. *Langmuir* **2006**, *22*, 9994–10002.
- (74) Kovacevic, D.; van der Burgh, S.; de Keizer, A.; Stuart, M. A. C. *Langmuir* **2002**, *18*, 5607–5612.
- (75) Kovacevic, D.; van der Burgh, S.; de Keizer, A.; Stuart, M. A. C. *J. Phys. Chem. B* **2003**, *107*, 7998–8002.
- (76) Laugel, N.; Betscha, C.; Winterhalter, M.; Voegel, J.-C.; Schaaf, P.; Ball, V. *J. Phys. Chem. B* **2006**, *110*, 19443–19449.
- (77) Sukhishvili, S. A.; Kharlampieva, E.; Izumrudov, V. *Macromolecules* **2006**, *39*, 8873–8881.
- (78) Ramsden, J. J.; Lvov, M. Y.; Decher, G. *Thin Solid Films* **1995**, *254*, 246–251.
- (79) Hess, B.; Bekker, H.; Berendsen, H. J. C.; Fraaije, J. G. E. M. *J. Comput. Chem.* **1998**, *18*, 1463–1472.
- (80) Ryckaert, J.-P.; Bellemans, A. *Chem. Phys. Lett.* **1975**, *30*, 123–125.
- (81) Vishnyakov, A.; Neimark, A. V. *J. Chem. Phys.* **2008**, *128*, 164902.
- (82) Vishnyakov, A.; Neimark, A. V. *J. Phys. Chem. B* **2000**, *104*, 4471–4478.
- (83) Wick, C. D.; Martin, M. G.; Siepmann, J. I. *J. Phys. Chem. B* **2000**, *104*, 8008–8016.
- (84) Wang, L.; Yu, H. *Macromolecules* **1988**, *21*, 3498–3501.
- (85) Berendsen, H. J. C.; van der Spoel, D.; van Drunen, R. *Comput. Phys. Commun.* **1995**, *91*, 43–56.
- (86) Lindahl, E.; Hess, B.; van der Spoel, D. *J. Mol. Model.* **2001**, *7*, 306–317.
- (87) Levitt, M.; Hirshberg, M.; Sharon, R.; Daggett, V. *Comput. Phys. Commun.* **1995**, *91*, 215–231.
- (88) Mackerell, A. D.; Wiorkiewicz-Kuczera, J.; Karplus, M. *J. Am. Chem. Soc.* **1995**, *117*, 11946–11975.
- (89) Jorgensen, W. L.; Madura, J. D.; Swenson, C. J. *J. Am. Chem. Soc.* **1984**, *106*, 6638–6646.
- (90) Jorgensen, W. L.; Gao, J. *J. Phys. Chem.* **1986**, *90*, 2174–2182.

- (91) Reith, D.; Muller, B.; Muller-Plathe, F.; Wiegand, S. *J. Chem. Phys.* **2002**, *116*, 9100–9106.
- (92) Frank, M.; Burchard, W. *Makromol. Chem. Rapid Commun.* **1991**, *12*, 645–652.
- (93) Berendsen, H. J. C.; Postma, J. P. M.; Gunsteren, W. F.; Hermans, J. Interaction models for water in relation to protein hydration. In *Intermolecular forces*; Reidel: Dordrecht, 1981.
- (94) Miyamoto, S.; Kollman, P. A. *J. Comput. Chem.* **1992**, *13*, 952–962.
- (95) Spoel, D. V. D.; Lindahl, E.; Hess, B.; Groenhof, G.; Mark, A. E.; Berendsen, H. J. C. *J. Comput. Chem.* **2005**, *26*, 1701–1718.
- (96) Berendsen, H. J. C.; Postman, J. P. M.; van Gunsteren, W. F.; DiNola, A.; Haak, J. R. *J. Chem. Phys.* **1984**, *81*, 3684–3690.
- (97) Essmann, U.; Perera, L.; Berkowitz, M. L.; Darden, T.; Lee, H.; Pedersen, L. G. *J. Chem. Phys.* **1995**, *103*, 8577–8593.
- (98) Zhang, R.; Shklovskii, B. I. *Phys. A* **2005**, *352*, 216–238.
- (99) Allen, M. P.; Tildesley, D. J. *Computer simulation of liquids*; Oxford University Press: New York, 1987.
- (100) Gardlund, L.; Wagberg, L.; Norgren, M. *J. Colloid Interface Sci.* **2007**, *312*, 237–246.
- (101) Buscher, K.; Graf, K.; Ahrens, H.; Helm, C. A. *Langmuir* **2002**, *18*, 3585–3591.
- (102) Kato, N.; Schuetz, P.; Ferry, A.; Caruso, F. *Macromolecules* **2002**, *35*, 9780–9787.
- (103) Tanchak, O. M.; Yager, K. G.; Fritzsche, H.; Harroun, T.; Katsaras, J.; Barrett, C. J. *J. Chem. Phys.* **2008**, *129*, 084901.
- (104) Dobrynin, A. V.; Rubinstein, M. *Prog. Polym. Sci.* **2005**, *30*, 1049–1118.
- (105) Stolz, C.; de Pablo, J. J.; Graham, M. D. *J. Rheol.* **2006**, *50*, 137–167.
- (106) Hiemenz, P. C.; Rajagopalan, R. *Principles of Colloid and Surface Chemistry*; Marcel Dekker: New York, 1997.
- (107) Jusufi, A.; Hynninen, A.-P.; Panagiotopoulos, A. Z. *J. Phys. Chem. B* **2008**, *112*, 13783–13792.
- (108) Ju, S.-P.; Lee, W.-J.; Huang, C.; Cheng, W. Z.; Chung, Y. T. *J. Chem. Phys.* **2007**, *126*, 224901.